JOURNAL OF THERMOPHYSICS AND HEAT TRANSFER
Vol. 7, No. 4, Oct.–Dec. 1993

Vibrational Relaxation Measurements in an Expanding Flow Using Spontaneous Raman Scattering

Surendra P. Sharma* and Stephen M. Ruffin†
NASA Ames Research Center, Moffett Field, California 94035
and
Walter D. Gillespie‡ and Scott A. Meyer‡
Stanford University, Stanford, California 94305

Vibrational relaxation of nitrogen in a two-dimensional nozzle flow is studied with spontaneous Raman scattering. An electric arc-driven shock tube operating as a reflected shock tunnel produces stagnation conditions of 5600 K and 100 atm. A 248-nm KrF laser pulse is focused into the nozzle to produce spatially resolved spontaneous Raman spectra. Vibrational population distributions are derived from the spectra for the states $v = 0$ to $v = 8$. The experimental results are compared with two theoretical models: 1) the Landau-Teller relaxation model and 2) a numerical solution of the master equations using transition rates derived from Schwartz, Slawsky, and Herzfeld (SSH) theory. We have measured a value for the Landau-Teller correction factor (ϕ) to be 1.0–1.5.

I. Introduction

THE effects of vibrational nonequilibrium in shock waves and rapid expansions have been studied for over three decades. In early shock-tube experiments, investigators found that the vibrational energy behind a shock wave was not in equilibrium with the rotational and translational energy; i.e., the vibrational temperature was not in equilibrium with the rotational temperature. The Landau-Teller model adequately described the measured vibrational relaxation rates up to 6000 K.[1] This model, which is based on the harmonic oscillator, predicts linear relaxation through Boltzmann distributions. In expanding flows, however, the measured relaxation rates were faster than the Landau-Teller model predicted. By comparing the measured relaxation rate to the Landau-Teller prediction, a correction factor was defined as $\phi = \tau_{LT}/\tau_{\text{meas}}$. Reported values of ϕ varied from 5 to 70 for N_2 and from 1 to 1000 for CO.[2]

The discrepancy between the rates observed in shocks and expansions led to a re-evaluation of the Landau-Teller model. A more thorough analysis of vibrational excitation and deexcitation reveals that these processes are the result of vibrational-translational (V-T) exchanges and vibrational-vibrational (V-V) exchanges. In V-T exchanges, the collision energy must be comparable with the vibrational energy spacing, which is equivalent to 3390 K for $v = 0$–1 in nitrogen. Typically, V-V exchanges are nearly resonant, and the collision energy is generally much higher than the anharmonic difference in energy spacings. Consequently, V-T exchanges are more strongly dependent on the translational temperature than V-V exchanges.[3]

In shock waves, where most of the molecules begin in the vibrational ground state, V-T exchange for $v = 0$–1 is the rate limiting step. This behavior led Park[4] to propose the geometric average formulation $T_a = \sqrt{TT_v}$, where the relaxation is slow until the upper vibrational states become populated and V-V exchanges occur. On the other hand, expansions typically begin with significant vibrational excitation V-V exchanges are then more probable, and calculations show that the vibrational distribution can deviate from Boltzmann with overpopulation of the upper states.[5] Non-Boltzmann distributions were deduced from infrared emission spectra of CO expansions by Bender et al.[6] who found good agreement with calculations which included anharmonicity.

Vibrational relaxation in nitrogen expansions has received renewed attention in recent years. Two of the authors[7,8] have used SSH theory to predict V-V exchange rates. The transition rates calculated can lead to non-Boltzmann distributions in nitrogen expansions. However, the magnitude of the transition rates depends strongly on the interaction potential assumed for the calculation. The lack of experimental data on nitrogen prompted the current experimental work. Because nitrogen is infrared inactive, neither emission nor absorption spectra can be measured. Spontaneous Raman scattering has long been recognized as a direct technique for population measurements, but the small cross section for this process has made such measurements difficult. Using a KrF excimer laser at 248 nm and an intensified CCD camera, single-shot Raman spectra are recorded in a shock tunnel. These spectra are used to determine the population distribution at several stations along the axis of the nozzle and to study the overall relaxation of vibrational energy.

In a previous paper, holographic interferometry validated a two-dimensional computation of the bulk properties of the flowfield.[9] The same paper also described a quasi-one-dimensional code which solved the vibrational master equations down the nozzle. These codes are improved for the current work and used in the analysis of the Raman data. The two-dimensional code computes the bulk properties in a stream tube along the axis centerline, and the quasi-one-dimensional code uses the same stream tube to predict vibrational population distributions.

II. Experimental Facility and the Raman Diagnostics System

The nitrogen expansion studied in this experiment is generated in the test section of a reflected shock tunnel at the Electric Arc Shock Tube (EAST) facility at NASA Ames Research Center. The capabilities of the facility[10] are described in detail elsewhere and will only be described briefly

Presented as Paper 92-2855 at the AIAA 27th Thermophysics Conference, Nashville, TN, July 6–8, 1992; received July 28, 1992; revision received Dec. 8, 1992; accepted for publication Dec. 18, 1992.

*Research Scientist. Associate Fellow AIAA.
†Research Scientist. Member AIAA.
‡Graduate Student. Student Member AIAA.

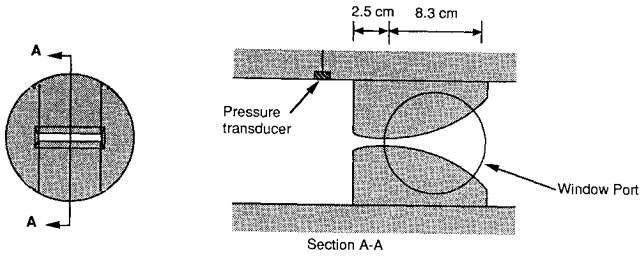

Fig. 1 Schematic of two-dimensional nozzle plug insert showing pressure transducer in reservoir and nozzle profile.

here. The aluminum driven section has an i.d. of 10 cm and is converted into a reflected shock tunnel with a nozzle plug insert installed 402 cm from the diaphragm as shown in Fig. 1. The plug insert has a large port for optical access on each side of the nozzle. This nozzle, with a throat height of 0.64 cm, is 8.3-cm long and has a quadratic profile downstream of the throat

$$(A/A^*) = 1 + (x/2.54\text{ cm})^2$$

where x is the distance from the throat in cm. Note that there is no secondary diaphragm at the nozzle entrance. The driven section is initially filled to 150 Torr with Matheson prepurified grade nitrogen. The cylindrical driver is 10 cm in diameter, 76-cm long, and is initially filled with 325-psia helium. The diaphragm is 3.2-mm thick 2024 zero temper aluminum with 60% groove depth and four petals.

The shock tube is fired by discharging a capacitor bank through a tungsten wire running along the centerline of the driver. The wire vaporizes and the current is carried by an arc in the driver gas, raising the temperature and pressure. The diaphragm bursts, creating a 2.6-km/s incident shock in the driven section. The shock reflects off the nozzle plug endwall, leaving stagnant nitrogen at approximately 5600 K and 100 atm. The shock-heated nitrogen then expands through the two-dimensional nozzle. The test ends with the arrival of a reflection from the contact surface which occurs about 175 μs after shock reflection at the endwall.

The vibrational population distribution at various nozzle stations is measured with spontaneous Raman scattering spectroscopy. Raman scattering is an inelastic scattering process in which light incident on a molecule is shifted in frequency as the molecule undergoes a transition to a new internal energy state. In general, energy may be transferred either from the incident photon to the molecule or vice versa, and these two cases are designated Stokes and anti-Stokes Raman, respectively. In this particular experiment, only the Stokes process is considered, and from the Stokes spectrum the Q-branch is of primary interest. The Stokes Q-branch designates the process in which the molecule gains a single quantum of vibrational energy from the photon without changing its rotational state. Because nitrogen is an anharmonic oscillator, the energy required to transition from a given vibrational state to the next higher level decreases with increasing vibrational level. The Raman shift from successively higher levels, then, will be very slightly smaller, but this difference is resolved in the present experiment. The intensity of Raman scattering is related in a simple way to the number density in each vibrational level and is a measure of the vibrational population distribution at the point where the Raman scattered light is collected.

The Raman spectra are excited with a KrF excimer laser (Lambda Physik EMG 150) operating at 248 nm. A 250 mJ, 25-ns pulse probes the test gas as shown in Fig. 2. The linewidth is 0.003 nm (manufacturers specification), and direct measurements of Rayleigh scattered light show that the linewidth is indeed smaller than the resolution of the spectrometer. Two $\lambda/4$ waveplates rotate the polarization of the horizontally polarized oscillator beam before it passes through

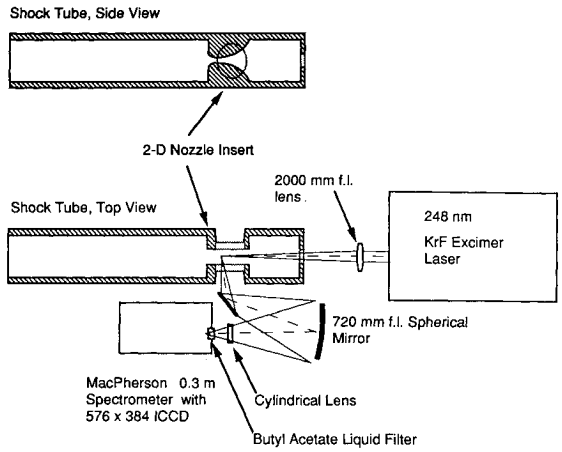

Fig. 2 Raman scattering layout. Laser beam is focused into test section and Raman scattered light is detected by spectrometer with intensified CCD camera.

the amplifier cavity. The amplified vertically polarized beam is at least 85% locked.

The arrival of the reflected shock from the endwall is detected by a piezoelectric pressure transducer (model PCB 113A24). This signal triggers a delay circuit which fires the laser after a 100-μs delay. The excimer beam is focused into a 6- × 0.1-mm sheet in the nozzle by a 2000-mm lens tilted nearly 45 deg to the beam. An f/5.3 spherical concave mirror collects the Raman scattered light, and a cylindrical lens corrects for astigmatism. Suprasil II windows and lenses were chosen to minimize fluorescence from the optics. This collection scheme images the focal volume of the beam onto the slit of a 0.3-m McPherson 218 spectrometer. The spectrometer is equipped with a 3600-ln/mm grating blazed at 2500 Å and an intensified CCD camera which provide spectral resolution of 0.1 nm. Background emission is rejected by gating the intensifier to operate only during the laser pulse. A butyl acetate filter of 1-cm pathlength placed near the entrance slit absorbs the Rayleigh scattered light before it enters the spectrometer.

The collection optics and spectrometer are mounted on rails so that the data can be taken at different stations along the nozzle centerline. The locations in the nozzle at which data are collected are determined to within 0.15 mm by illuminating a scale placed in the nozzle with an atomic line source, opening the spectrometer slits, and observing the digitized image of the scale from the intensified CCD (ICCD). Although submillimeter spatial resolution for the Raman spectra is possible, low signal levels require that the spectra be integrated over the spatial dimension by summing the columns of the ICCD array into "superpixels." This limits the spatial resolution to 0.88 cm. In addition to taking measurements along the nozzle, the system can also be configured to collect spectra in the stagnation region with some reduction in collection efficiency.

III. Numerical Models

The nozzle flowfield is computed using two different computational schemes. A two-dimensional Navier-Stokes calculation is performed to predict boundary-layer effects and effects due to vertical and streamwise velocity components in the rapidly expanding nozzle. The two-dimensional code utilizes the standard Landau-Teller relaxation equation to predict energy transfer from the vibrational to translational modes. The second type of code used can solve the vibrational master equations to determine vibrational energy transfer, but solves the quasi-one-dimensional fluid dynamic equations. The two-dimensional flow solution is used to determine an effective quasi-one-dimensional nozzle contour. This effective nozzle contour is used in the quasi-one-dimensional calculations. Details of this procedure are given in subsequent paragraphs.

A. Two-Dimensional Nozzle Calculations

Calculations of the thermochemical nonequilibrium nozzle flowfield were performed with a modified version of the code developed by Palmer.[11] The present code is also an improved version of the code used in Ref. 9. The solver has fully coupled finite-rate chemistry, upwind differencing, and an explicit time-marching solution algorithm. In the present study, the species concentrations of N_2 and N are solved using the two-temperature $\sqrt{TT_v}$ model and reaction rates obtained from Park.[4] Binary diffusion is assumed and the vibrational energy transfer rate is determined by the original Landau-Teller model.

In order to provide adequate resolution of the boundary layer, especially in cold wall simulations, second-order accurate spatial differencing is required. Even with second-order accuracy, however, the van Leer flux splitting used in Refs. 9 and 11 resulted in large numerical dissipation in the boundary layer for cold wall simulations. For the present calculations, a second-order accurate Roe's averaged flux differencing scheme was used. This scheme is similar to the flux differencing scheme used by Obayashi[12] and gave much more accurate boundary-layer representations than the van Leer scheme for cold wall cases.

The inflow plane for the two-dimensional nozzle computations is just downstream of the shock reflection wall of the nozzle insert. An equilibrium chemical composition is assumed, and vibration is assumed to be in equilibrium with the translational and rotational modes. At this station, total pressure, total temperature, and flow angle are specified and a subsonic characteristic boundary condition is enforced. The nozzle calculations were performed on a 32 × 23 grid and the initial flow condition specified was uniform flow.

B. Quasi-One-Dimensional Calculations

To study the details of the vibrational relaxation process, one must solve vibrational master equations. However, calculation of all the transition probabilities and rates even for one temperature is computationally expensive. In a general two- or three-dimensional flow it would be necessary to compute these for every temperature in the flowfield and to solve the vibrational rate equation for each vibrational level and the fluid dynamic equations simultaneously. Thus, detailed calculations of the vibrational transition rate equations in general two- or three-dimensional flows are prohibitively expensive. However, quasi-one-dimensional calculations require much less CPU time than two- or three-dimensional calculations because the number of grid nodes and equations are reduced.

The quasi-one-dimensional code used in the present study is similar to that described by Ruffin and Park.[8] However, the present version includes finite-rate chemistry, and the quasi-one-dimensional solutions presented use the same N_2 reaction rates as the two-dimensional code previously described. Although the coupling of vibrational energy to dissociation rate is only approximated by use of the Park $\sqrt{TT_v}$ model, the approximation is justified: for the present conditions, the flow is only weakly dependent on the dissociation rate. This weak dependence on the flow chemistry is due to the near frozen chemical conditions of the present expanding flow.

The quasi-one-dimensional code solves the vibrational master equations to determine vibrational population distributions and vibrational energy transfer. The vibrational transition rate master equations are of the form

$$\frac{\mathrm{D}(N_v/\rho)}{\mathrm{D}t} = \left(\frac{N}{\rho}\right) \sum_{v'=0}^{v_{\max}} (K_{v',v}N_{v'} - K_{v,v'}N_v)$$

where N_v is the number of molecules in state v per unit volume. $K_{v',v}$ is the vibrational transition rate found from SSH theory. The fluid transport relations can then be used to convert the material derivative to finite volume form

$$\frac{\partial N_v}{\partial x} = \left(\frac{N}{u}\right) \sum_{v'=0}^{v_{\max}} (K_{v',v}N_{v'} - K_{v,v'}N_v) - \frac{N_v}{A}\frac{\mathrm{d}A}{\mathrm{d}x} - \frac{N_v}{2u^2}\frac{\partial(u^2)}{\partial x}$$

The streamwise velocity is u and the nozzle cross-sectional area is A.

Although the quasi-one-dimensional approximation has been made, the use of typical time marching numerical schemes for solving the finite difference form of the governing equations would still be computationally very expensive. However, advantage can be taken of the quasi-one-dimensional formulation by performing one spatial march rather than iterating in time. For this study, an efficient, implicit, space marching solver called STIFF7 is used. STIFF7 numerically computes jacobians and integrates a coupled set of quasi-linear, partial differential equations and is described in detail by Lomax.[13] The above transition rate and energy relaxation equations are coupled with the fluid dynamic equations for quasi-one-dimensional, steady-state flow. The use of STIFF7 in nozzle flow computations and additional details of the present quasi-one-dimensional solver are given by Ruffin and Park.[8] The present solver is used to also investigate the performance of the Landau-Teller equation. This is done by omitting the population distribution equations and using the Landau-Teller relaxation equation instead of the true energy rate equation.

The quasi-one-dimensional approximation used herein is valid for steady-state inviscid flows in which the flow area changes gradually. In this study, an effective nozzle contour which meets these requirements is obtained from a solution of the two-dimensional Navier-Stokes equations. The effective quasi-one-dimensional nozzle contour obtained as described below allows the quasi-one-dimensional code to give the same prediction as the centerline solution of the two-dimensional Navier-Stokes code. Figure 3a shows normalized density contours and a selected stream tube from the two-dimensional solution using the code described in the previous section. The rapid turning near the wall is caused by the thermal boundary layer which is influenced by the cold wall

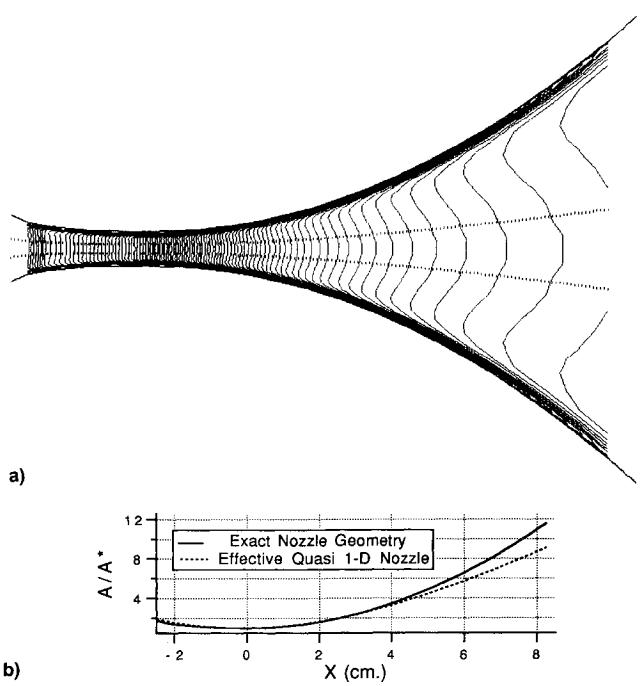

Fig. 3 a) Density contours from two-dimensional nozzle calculations showing quasi-one-dimensional flow in stream tube along the centerline, b) comparison of effective quasi-one-dimensional area ratio to exact nozzle geometry.

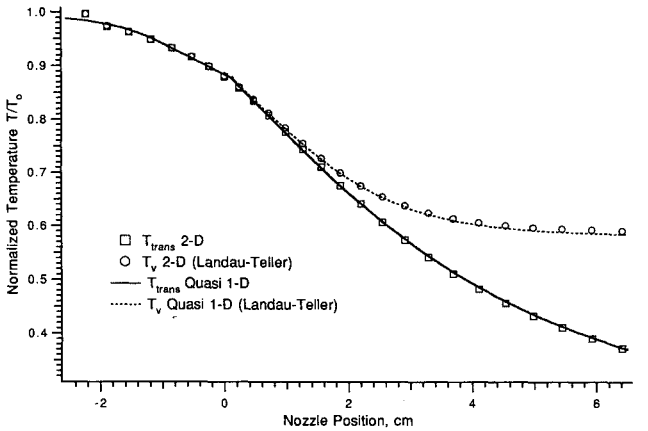

Fig. 4 Comparison of two-dimensional computational results to quasi-one-dimensional results with the effective nozzle geometry correction.

boundary condition. The more gradual curve of the contours, especially near the nozzle exit, illustrates that the core inviscid flow is very two-dimensional in that region. Near the throat region, the density contours are nearly vertical which indicates that in that region the inviscid flow is nearly uniform. Figure 3a also shows one stream tube near the centerline of the nozzle. The stream tube selected has a slowly expanding area and is in a purely inviscid region of the flow. Within this stream tube, the flow at each streamwise station is nearly uniform and the flow angle is never greater than 10 deg. This stream tube satisfies the requirements for the quasi-one-dimensional approximation and is used as the effective quasi-one-dimensional nozzle contour. A comparison of the true nozzle area ratios to the effective nozzle area ratios is given in Fig. 3b. The effective nozzle area ratio is identical to the true nozzle area ratio near the throat, but expands more slowly near the downstream end of the nozzle. The effective nozzle contour used in the present quasi-one-dimensional computations is given by

$$A/A^* = 1 + x/C_1 + x^2/C_2 + x^3/C_3$$

where

$$C_1 = 26.1962$$

$$C_2 = 6.4811$$

$$C_3 = -206.0117$$

The effective quasi-one-dimensional nozzle contour shown in Fig. 3 is defined so that a quasi-one-dimensional solution on the effective nozzle matches the centerline solution from the two-dimensional Navier-Stokes code. Figure 4 shows a comparison of the quasi-one-dimensional vibrational and translational temperatures to the centerline values of the two-dimensional solution. We see that the use of the effective quasi-one-dimensional nozzle contour in the quasi-one-dimensional code gives solutions with are in excellent agreement with the two-dimensional viscous solution.

IV. Results

A. Shock Tunnel Measurements

Since Raman data can only be collected at a single point in the nozzle during a run, a series of runs is made with the same initial conditions in order to assemble a full set of data. Although the flow in the shock tube is remarkably reproducible, even the small variations seen in shock speed (~3%) lead to nonnegligible differences in the stagnation conditions from run to run. For this reason, the progress of the shock is closely monitored in every run. Four ionization probes measure time of arrival of the shock wave at four stations in the shock tube, while two photomultiplier tubes are used to detect the arrival of the mixing region (contact surface) at two of the measurement stations. These measurements indicate that about 150 μs of test flow is available behind the incident shock. Some attenuation in shock speed is noted, roughly 0.12 mm/μs/m.

A typical pressure trace from the station 2.54-cm upstream of the endwall is shown in Fig. 5. The features of this pressure trace are 1) the arrival of the incident shock followed by a region of constant pressure, 2) the arrival of the first leg of the bifurcated reflected shock, 3) the second leg of the bifurcated reflected shock including an overshoot, 4) a period of relatively constant pressure, and 5) a drop in pressure associated with an expansion emanating from the contact surface upstream from the measurement station. Note that since the bifurcation of the reflected shock is limited to the region of the boundary layer, the period of constant conditions behind the reflected shock includes at least the time from the arrival of the first leg of the bifurcated shock to the time of arrival of the expansion from the contact surface, about 175 μs. This time minus the startup time of the nozzle, about 80 μs, is the testing time for the facility. The measured pressure behind the reflected shock is taken to be the average pressure during the approximately 75-μs plateau in the pressure trace.

The best correlation between shock speed and measured pressure behind the reflected shock is achieved using a linear fit to the three time-of-arrival measurements nearest the end of the shock tube. This correlation is shown in Fig. 6. The systematic offset between measured and computed pressures behind the reflected shock for a given shock speed can be

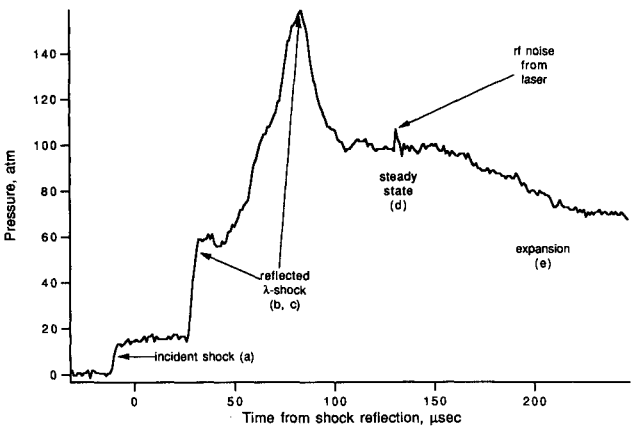

Fig. 5 Reservoir pressure 2.54 cm from endwall showing incident and reflected shocks, test time, and arrival of the expansion wave.

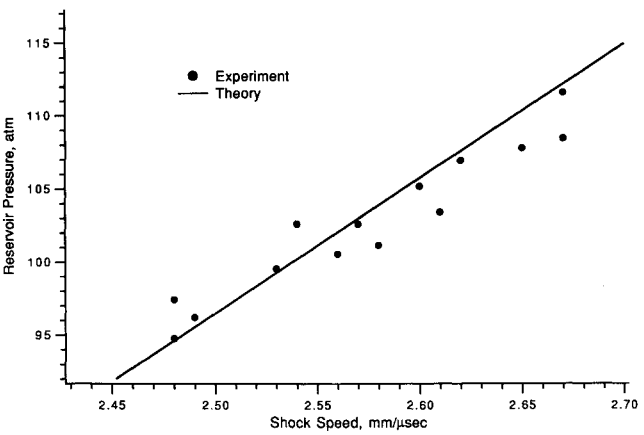

Fig. 6 Comparison between measured reservoir pressure and shock speed to theoretical calculations based on the Rankine-Hugoniot relations.

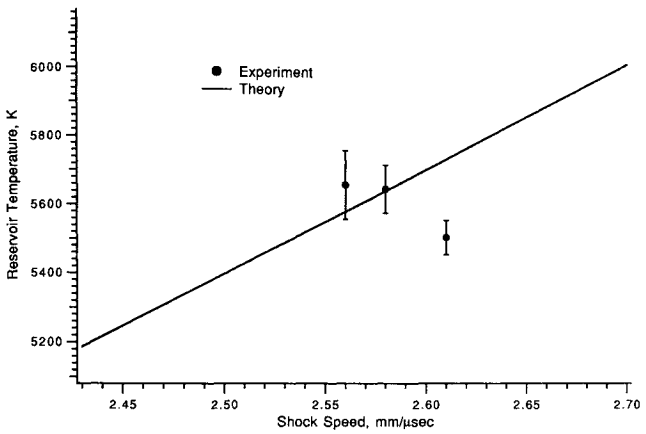

Fig. 7 Comparison between measured reservoir temperature and theoretical calculations based on effective shock speed.

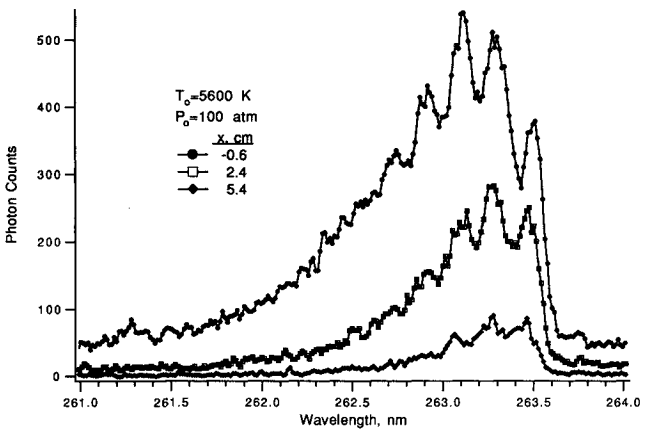

Fig. 8 Raman spectra taken at three stations along the nozzle centerline. Distances measured from the throat.

attributed to nonidealities in reflected shock tube operation such as shock attenuation (boundary-layer growth) and three-dimensional effects in the shock reflection. These nonidealities are accounted for by defining an effective shock speed. This effective shock speed is 0.03 mm/μs slower than the measured shock speed.

The temperature in the reservoir region behind the reflected shock was measured using the same spontaneous Raman technique applied in the nozzle. Figure 7 shows the three measurements which were made, two of which agree well with Rankine-Hugoniot predictions for temperature behind the reflected shock. This is considered sufficient agreement to justify using calculated temperatures based on the effective shock speed for reservoir temperatures. In this way, run-to-run variations in reservoir conditions are accounted for in the data analysis. It should be stressed that these corrections are relatively minor, and, while they do reduce the scatter in the data, they do not significantly alter the conclusions.

B. Raman Measurements

The probing laser beam was focused into a thin sheet of 0.1 × 6.0 mm to avoid gas breakdown in the focal volume, while at the same time maximizing the light collected by the detection system. Experimentation with various focal spot sizes and laser intensities demonstrated the energy density of the beam in the focal volume did not measurably perturb the spectra, nor were coherent Raman processes observed.

Raman spectra taken from three of the seven stations along the nozzle axis are shown in Fig. 8. The columns of pixels on the two-dimensional ICCD array are binned to form superpixels, each of which is designated by a symbol in the spectrum. Although each superpixel represents the Raman signal averaged over an 0.88-cm path length, the variation in vibrational temperature over this distance is smaller than the experimental error for the measurement, as will be shown below. The abscissa is scaled to approximate the number of photons detected for each superpixel so that, for example, at $x = -0.6$ cm we see that a total of about 30,000 Raman scattered photons are detected. As expected, the Raman signal drops as the number density drops along the nozzle. Looking at the number of vibrational peaks present, it is also noted that the vibrational energy of the flow is dropping as the gas expands.

The Raman spectra are analyzed first by deducing vibrational population distributions. Since the overlap between adjacent levels is dependent on the rotational temperature, and since low signal levels preclude the measurement of rotational temperature from the Raman spectra, an estimate for the rotational temperature based on the two-dimensional flowfield computations is made. This estimate for the rotational temperature has very little impact on the evaluation of a vibrational relaxation model since the computed rotational

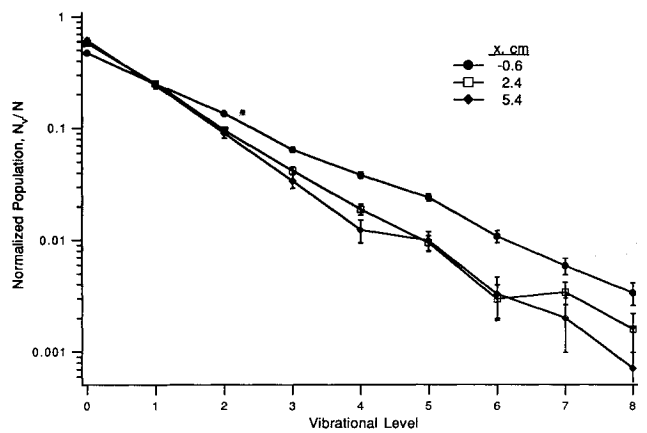

Fig. 9 Boltzmann plot of measured vibrational population distribution at three stations along the nozzle centerline. Distances measured from the throat.

temperatures in the expansion are virtually independent of the vibrational relaxation model used, and furthermore, the vibrational distributions are relatively insensitive to the rotational temperature.

The procedure for generating population distributions from the experimental spectra is begun by simulating a separate Raman spectrum for each vibrational level. Each simulated Q-branch (spectrum of an individual vibrational level) is divided into wavelength intervals roughly corresponding to the peaks of a complete spectrum. The intensity is integrated within each interval to yield a factor quantifying the contribution of each vibrational level to the given wavelength interval. For each run, an entire matrix of these overlap factors is constructed. This matrix is then inverted and multiplied with a vector constructed from the measured integrated intensities within each wavelength interval. The result is the intensity of each of the vibrational levels from the experimental spectrum.

For spontaneous Raman, the intensity of each level is proportional to the population in that level scaled by the level plus one, i.e.

$$I_v \sim N_v(v + 1)$$

The intensities are divided by the factor $(v + 1)$, and the distribution is normalized by the sum of all the levels to yield the relative vibrational population distribution.

The resulting population distributions are shown on a Boltzmann plot in Fig. 9. The lower vibrational states fit well along a straight line, indicating a Boltzmann distribution. An alternative representation of the same data is shown in Fig. 10. A vibrational temperature for each level (Θ_v) is defined by

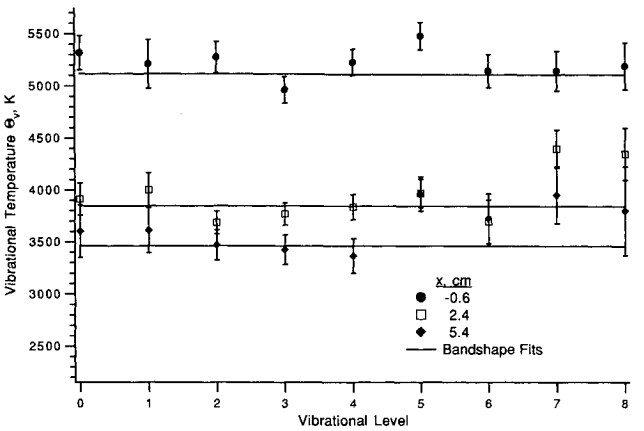

Fig. 10 Vibrational temperature of individual vibrational levels derived from the relative populations.

the population ratio of that level to the ground state, i.e.

$$N_v/N_0 = \exp[-(E_v - E_0)/k\Theta_v]$$

and the ground state vibrational temperature is defined as

$$N_0/N = \frac{\exp(-E_0/k\Theta_0)}{Q}$$

where the partition function has been approximated by

$$Q = \frac{\exp(-E_0/k\Theta_0)}{1 - \exp(-\Delta E_0/k\Theta_0)}$$

For these test conditions, SSH theory predicts a small overpopulation of the very high-vibrational states ($v > 20$). However, the absolute number densities of the upper states are so small that the *S/N* (signal-to-noise ratio) is less than 1 for states above $v = 8$. Although there is some scatter and uncertainty in the data for the vibrational levels 5–8, the distributions are nearly Boltzmann, and a single vibrational temperature is a good approximation for the levels measured.

Instead of deducing a single vibrational temperature from the vibrational distributions, better accuracy is obtained by using a band-shape fitting technique and assuming a Boltzmann distribution for $v = 0$–8. This technique consists of iteratively synthesizing Raman spectra for different vibrational temperatures and comparing to the measured spectra. The temperature for which the best match is achieved is taken to be the measured vibrational temperature. Again, the measured temperature is dependent to some degree on the rotational temperature which is an independent input to the synthesized spectrum. The rotational temperature is estimated from the two-dimensional computation and held fixed in the band-shape fitting as the vibrational temperature is varied.

Substantial effort was required to achieve adequate *S/N* in the experiment. The gain on the intensified CCD camera was adjusted so that single photoelectrons could be detected. Based on photon count levels, the measured Raman signal levels agree reasonably well with estimates based on cross sections for spontaneous Raman found in the literature. Nevertheless, the data are limited primarily by photon statistical noise. Background emission and scattering levels were measured in time integrated spectra and were found to be smaller than the shot noise for the experiment, with the exception of emission from isolated spectral lines seen in the stagnation region and near the throat of the nozzle. The emission features were identified as iron lines and were not of sufficient intensity to affect the results of the experiment.

In the shot noise limited case, the *S/N* can be estimated by knowledge of the number of photons reaching the ICCD and the quantum efficiency. In the data analysis, the estimated *S/N* provides error bars for the populations on the Boltzmann plots and the vibrational temperatures deduced from band fit. Simulated spectra, which included artificial shot noise, have been analyzed by the same data reduction technique as the experimental spectra (see Fig. 11), and the resultant errors agree well with the error bars. More significantly, simulated spectra have also been used to evaluate the systematic error produced by errors in the calculated rotational temperature. The results in Fig. 12 are typical and show that an error of 100 K in the rotational temperature causes only a 40 K error in the vibrational temperature. Since the rotational temperature is nearly independent of the vibrational relaxation model used, the uncertainty in the rotational temperature is small. Because this small uncertainty leads to even smaller errors in the deduced vibrational temperature, errors in the computed rotational temperature are not a significant source of error in the vibrational temperature measurements.

The results for the vibrational temperature measurements are shown in Figs. 13 and 14 for all seven stations in the nozzle. At least two measurements were made at each station. The data has been normalized by the stagnation temperatures inferred from shock speed measurements as discussed above. Included in this plot are curves from the quasi-one-dimensional computations using the SSH and Landau-Teller models. Only a single curve is included for translational temperature since all calculations yield virtually identical results for this property.

The experimental data do not fall along a single line, yet the overwhelming evidence shows a relaxation rate that is reasonably well described by the simple Landau-Teller relaxation, and certainly is not much faster than Landau-Teller. Based on these results, an upper limit of 1.5 can be placed

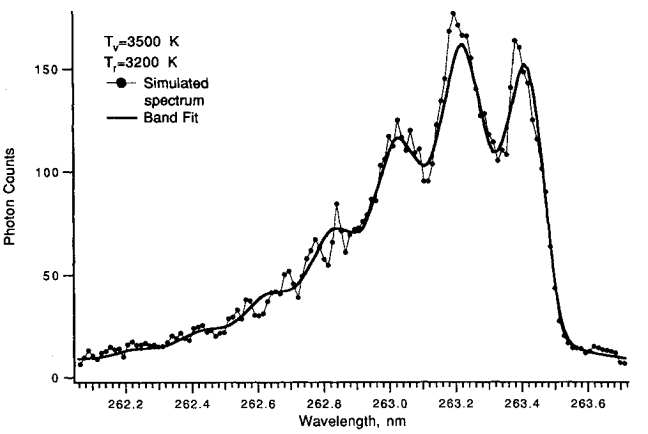

Fig. 11 Comparison of simulated spectrum to band-shape fit.

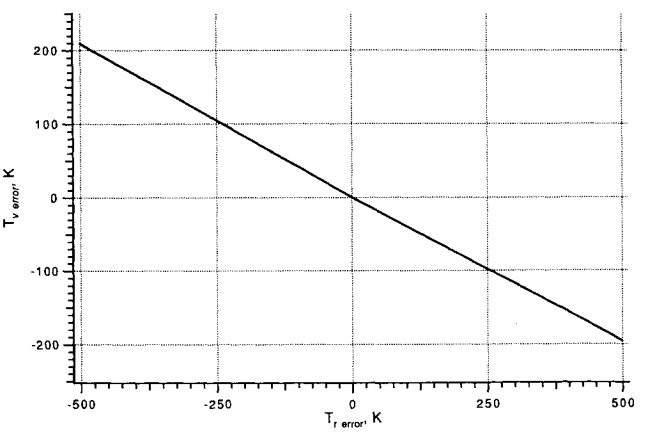

Fig. 12 Systematic error in vibrational temperature caused by uncertainty in rotational temperature.

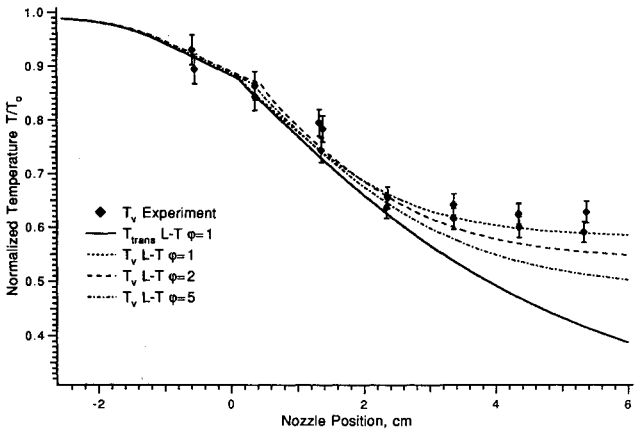

Fig. 13 Normalized temperatures along the centerline of the nozzle: experimental results compared to Landau-Teller relaxation with ϕ = 1, 2, and 5.

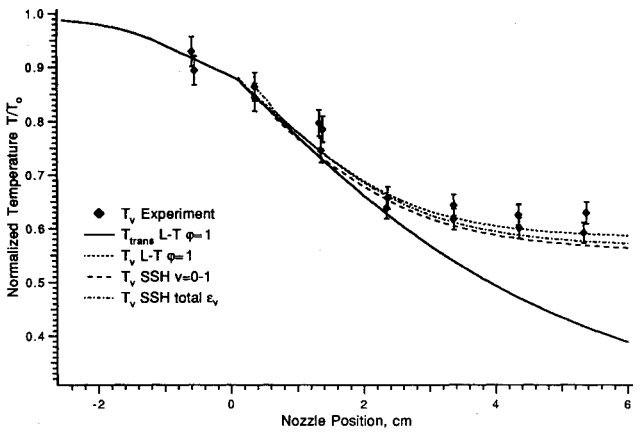

Fig. 14 Normalized temperatures along the centerline of the nozzle: experimental results compared to SSH relaxation model.

on ϕ. Furthermore, SSH theory also predicts the correct relaxation rate. The scatter in the data is believed to stem primarily from two sources: 1) some uncertainty in the reservoir conditions and 2) a degree of unsteadiness in the nozzle flow which may be seen as a temporally and spatially varying perturbation to the steady test flow. Pressure traces and holographic interferograms taken in the nozzle flow demonstrate that while some unsteadiness exists, it is a small fraction of the local flow properties.

The value of ϕ measured in the present experiment is considerably lower than previous estimates which lie in the range 5–70. This study differs from previous work with nitrogen in two important ways. First, spontaneous Raman scattering provides a direct measurement of the vibrational population. In past experiments, the flow was either seeded with thermometric species such as CO or sodium, or an electron beam was used to excite the nitrogen into an electronically excited state where it would radiate. Second, it is well-known that the presence of even a small amount of impurity can significantly increase the relaxation rate,[2] and the purity of the test gas is very important. In this experiment, seeding is not required to monitor the flowfield. The present experiment, therefore, represents the first direct measurement of vibrational energy in a spectroscopically clean flow.

V. Conclusions

The vibrational population distribution in an expanding flow of nitrogen has been measured directly using spontaneous Raman scattering. For the vibrational states measured, the population distribution is adequately modeled by a single vibrational temperature. A comparison of the measured vibrational temperature profile in the nozzle with computations shows good agreement to theory. The results show that both the Landau-Teller model and the SSH model describe the relaxation well. At these test conditions, the data indicates an upper limit of 1.5 on the relaxation correction factor ϕ.

Acknowledgments

The authors thank Edward H. Piepmeier for the design of the collection optics and for his invaluable assistance. His work was supported under the NASA-ASEE-Stanford Summer Fellowship Program.

References

[1]Millikan, R. C., and White, D. R., "Systematics of Vibrational Relaxation," *Journal of Chemical Physics*, Vol. 39, Dec. 1963, pp. 3209–3213.

[2]Hurle, I. R., "Nonequilibrium Flows with Special Reference to the Nozzle-Flow Problem," *Proceedings of the 8th International Shock Tube Symposium*, Imperial College, London, July 1971, pp. 3-1–3-37.

[3]Treanor, C. E., Rich, J. W., and Rehm, R. G., "Vibrational Relaxation of Anharmonic Oscillators with Exchange-Dominated Collisions," *Journal of Chemical Physics*, Vol. 48, Feb. 1968, pp. 1798–1807.

[4]Park, C., "A Review of Reaction Rates in High Temperature Air," AIAA Paper 89-1740, Buffalo, NY, July 1989.

[5]Caledonia, G. E., and Center, R. E., "Vibrational Distribution Functions in Anharmonic Oscillators," *Journal of Chemical Physics*, Vol. 55, July 1971, pp. 552–561.

[6]Bender, D. J., Mitchner, M., and Kruger, C. H., "Measurement of Vibration Population Distributions in a Supersonic Expansion of Carbon Monoxide," *Physics of Fluids*, Vol. 21, July 1978, pp. 1073–1085.

[7]Sharma, S. P., Huo, W. M., and Park, C., "The Rate Parameters for Coupled Vibration-Dissociation in a Generalized SSH Approximation," AIAA Paper 88-2714, San Antonio, TX, June 1988.

[8]Ruffin, S. M., and Park, C., "Vibrational Relaxation of Anharmonic Oscillators in Expanding Flows," AIAA Paper 92-0806, Reno, NV, Jan. 1992.

[9]Sharma, S. P., Ruffin, S. M., Meyer, S. A., and Gillespie, W. D., "Density Measurements in an Expanding Flow Using Holographic Interferometry," AIAA Paper 92-0809, Reno, NV, Jan. 1992.

[10]Sharma, S. P., Gillespie, W. D., and Meyer, S. A., "Shock Front Radiation Measurements in Air," AIAA Paper 91-0573, Reno, NV, Jan. 1991.

[11]Palmer, G., "Enhanced Thermochemical Nonequilibrium Computations of Flow Around the Aeroassist Flight Experiment Vehicle," AIAA Paper 90-1702, Seattle, WA, June 1990.

[12]Obayashi, S., "Numerical Simulation of Underexpanded Plumes Using Upwind Algorithms," *Proceedings of the AIAA Atmospheric Flight Mechanics Conference*, AIAA Paper 88-4360, Minneapolis, MN, Aug. 1988, pp. 284–299.

[13]Lomax, H., "Stable Implicit and Explicit Numerical Methods for Integrating Quasi-Linear Differential Equations with Parasitic-Stiff and Parasitic-Saddle Eigenvalues," NASA TN D-4703, May 1968.